





Efficient Two-Phase Multiobjective Sparse Unmixing Approach for Hyperspectral Data

Xiangming Jiang , Maoguo Gong , *Senior Member, IEEE*, Tao Zhan , Kai Sheng, and Mingliang Xu 

Abstract—In our previous work, a two-phase multiobjective sparse unmixing (Tp-MoSU) approach has been proposed, which settled the regularization parameter issues of the regularization unmixing methods. However, Tp-MoSU has limited performance in identifying the real endmembers from the highly noisy data in the first phase and cannot effectively exploit the spatial-contextual information in the second phase because of the similarity measure it used. To settle these two problems, a composite spectral similarity measure is first constructed by fusing the spectral correlation angle and the Euclidean distance. It is used instead of the Frobenius norm to measure the unmixing residuals in the first phase because it considers both the shape and amplitude discrepancy between two spectra simultaneously. Then, the $L_{2,\infty}$ norm is used instead of the l_2 norm to measure the unmixing residuals in the second phase, and the initialization, recombination, mutation, and local search strategies are also elaborately redesigned to help reduce this new objective, based on which the unmixing tasks of all pixels in a hyperspectral image can be completed at once. Therefore, this new measure facilitates the estimation of the abundances as a whole, and thus, the spatial-contextual information can be better exploited to improve the estimated abundances. Besides, the time efficiency for abundance estimation is also greatly improved. Experimental results demonstrate that the proposed method (termed as Tp-MoSU+) outperforms Tp-MoSU in both of the two phases under heavy noise and outperforms the tested regularization algorithms in estimating the abundances.

Index Terms—Composite spectral similarity measure, highly noisy data, $L_{2,\infty}$ norm, multiobjective sparse unmixing, spatial-contextual information, time efficiency.

I. INTRODUCTION

HYPERSPECTRAL imaging is currently able to acquire tens to hundreds of contiguous spectral bands, which provide much more information about a scene than the spaced spectral bands obtained by multispectral imaging, not to mention the

RGB image, which contains only three bands [1]. This attribute facilitates the identification and classification of objects [2], [3], and the analysis of potential substances in hyperspectral scene via the spectroscopic technique. Thus, the hyperspectral image has been widely used in the environmental monitoring [4], mineral exploration [5], surveillance [6], biomedical and biometric applications [7], [8], etc. Unfortunately, hyperspectral imaging cannot be implemented at a pure pixel level under the current conditions due to the insufficient spatial resolution of sensors, so most pixels in hyperspectral imagery are mixed [1], [9]. Therefore, spectral unmixing is in great demand to disclose the underlying materials, which jointly occupy each mixed pixel.

Under different simplified scattering assumptions, the spectral signatures of different materials are mixed in either linear or nonlinear manner [9]. If the secondary reflections and/or multiple scattering effects are negligible as opposed to the primary scattering in the data collection procedure [10], the linear mixing will dominate the mixing process [1]; otherwise, the nonlinear mixing will dominate. Although there is a growing trend of focus on the nonlinear mixing recently, the linear mixing is still widely investigated in many works [10] because of its computational tractability and flexibility [11].

A linear mixing model (LMM) assumes that the detected spectrum of one pixel in a hyperspectral imagery can be expressed as a linear combination of pure spectral signatures of the materials contained in it [1]. Therefore, the task of linear unmixing is to identify a collection of pure spectral signatures (*endmembers*), together with their combination coefficients (*abundances*), which indicate their respective proportion in that pixel. To meet the physical interpretability, the abundances of materials for each pixel are usually constrained to be nonnegative and sum-to-one, which are simply denoted as ANC and ASC [12], respectively. As indicated in [13], the statistical dependence of abundances ensured by the ASC, together with the high dimensionality of the hyperspectral data, makes hyperspectral unmixing (HU) out of reach for most classical source separation algorithms. The existing HU methods can be classified into geometrical based, statistical based, and sparse regression based according to [9].

Geometrical-based approaches attempt to identify the vertices of a simplex, which happen to span the hyperspectral data space, as endmembers either with [14] or without [15] the pure pixel assumption. However, this kind of approach has poor performance on highly mixed spectra [16]. In this case, the statistical-based approaches are viable alternatives at an extra cost of computational complexity. Statistical-based approaches

Manuscript received August 15, 2020; revised November 13, 2020 and January 5, 2021; accepted January 22, 2021. Date of publication January 28, 2021; date of current version February 18, 2021. This work was supported in part by the National Natural Science Foundation of China under Grant 62036006, and in part by the Key Research and Development Program of Shaanxi Province under Grant 2018ZDXM-GY-045. (*Corresponding author: Maoguo Gong.*)

Xiangming Jiang and Maoguo Gong are with the School of Electronic Engineering, Key Laboratory of Intelligent Perception and Image Understanding of Ministry of Education, Xidian University, Xi'an 710071, China (e-mail: OMEGAJiangXM@gmail.com; gong@ieee.org).

Tao Zhan is with the School of Computer Science and Technology, Key Laboratory of Intelligent Perception and Image Understanding of Ministry of Education, Xidian University, Xi'an 710071, China (e-mail: omegazhant@gmail.com).

Kai Sheng is with the Academy of Advanced Interdisciplinary Research, Xidian University, Xi'an 710071, China (e-mail: shengkaicn@hotmail.com).

Mingliang Xu is with the School of Information Engineering, Zhengzhou University, Zhengzhou 450001, China (e-mail: iexumingliang@zzu.edu.cn).

Digital Object Identifier 10.1109/JSTARS.2021.3054926

use a posterior estimation of unknowns (endmembers and abundances) as the inference engine to impose priors and model the statistical variability so that the final solution has physical meaning [9]. The sparse-regression-based approach has been proposed in the past ten years benefiting from the increasingly available spectral libraries. This kind of approach assumes that the underlying endmembers in the mixed pixels are included in an overcomplete spectral library known *a priori*; spectral unmixing is thus reduced to a sparse regression problem with respect to the abundances using the overcomplete spectral library. This attribute is attractive since the correct estimation of endmembers, which is a difficult task, is eliminated. Because the abundances of endmembers for each pixel are constrained by ASC and ANC, and the spectral signatures in a spectral library tend to be highly correlated, the sparse regression problem cannot be well solved by the standard sparse regression algorithms, which has been confirmed by the experiments in [12].

In order to explore the capacity of sparse regression in HU, a great variety of regularization approaches have been proposed successively. These approaches generally optimize a linear weighted function consisting of an unmixing residual term, a sparse regularizer, and/or a spatial regularizer derived from prior information. Commonly used unmixing residual terms include the l_2 norm based [13], l_1 norm based [17], and $l_{2,1}$ [18] norm based in order to better handle the Gaussian noise, impulse noise, stripe noise, and outliers in hyperspectral data. As for the sparse regularizer, the l_1 norm was first used instead of the l_0 norm to induce sparse abundance matrix [10], [13] because the l_0 -norm-based regularizer is nonconvex and hard to optimize. Then, the $l_{2,1}$ norm was given preference to induce sparse rows in the abundance matrix [19] based on the finding that all pixels of an image share a small set of endmembers in the spectral library. In order to study the utilization of the spatial information in estimating abundance, both the local and global spatial regularizers have been successfully established. The local spatial regularizers such as the total variation (TV) regularizer [20] and the multiscale spatial regularizer [21] were established based on the fact that the adjacent pixels are possibly similar in components and their proportions, while the global spatial regularizers such as the nonlocal means regularizer [22], [23] were established to exploit similar patterns throughout the whole image. A patch-based spatial-spectral kernel method proposed in [24] can even capture the homogeneous neighborhood adaptively to exploit the spatial-spectral information as much as possible. Furthermore, researchers are proposing more and more regularizers of various forms to exploit the spatial-spectral information more flexible such as the rolling-guidance-based regularizer [25] and the weighted nonlocal low-rank tensor [26], etc. All these approaches have achieved promising unmixing results, but they need to select suitable regularization parameters and require the convexity and differentiability of their objective functions.

In fact, the sparse unmixing problem is essentially a multiobjective optimization problem because minimizing unmixing residuals, inducing sparsity, and exploiting spatial information with regard to the abundance matrix are three conflicting objectives. In [27], we proposed a multiobjective sparse unmixing

method and designed an effective cooperative coevolutionary algorithm for it, but the computational complexity is unsatisfactory especially when an image has tens of thousands of thousands of pixels. A multiobjective optimization method based on NSGA-II was proposed in [28], which used flipping to identify the real endmembers. However, the gene exchange among individuals was not considered, and the nondominated sorting strategy used in NSGA-II was time-consuming. Thereafter, different multiobjective-optimization-based unmixing methods were proposed by introducing spectral priors or spectral processing techniques into the multiobjective modeling and optimizing and optimizing processes, e.g., the spectral- and multiobjective-based sparse unmixing [29], the classification-based model for multiobjective sparse unmixing [30], and the dictionary-pruning-based multiobjective sparse unmixing [31]. In our previous work, we proposed a two-phase multiobjective sparse unmixing (Tp-MoSU) method [32], which identifies the real endmembers and estimates abundances in two phases. In each phase, a biobjective optimization problem was established to optimize the unmixing accuracy and the objective derived from prior information. Tp-MoSU exhibited good performance in identifying real endmembers and estimating abundances in most cases, but it still has limitations. In the first phase, Tp-MoSU has limited performance in identifying the real endmembers under heavy noise because the unmixing residuals measured by the Frobenius norm (F -norm) are sensitive to the gain and offset of the spectral amplitude caused by heavy noise. In the second phase, limited by the optimization ability of the constructed objective and the designed algorithm, the abundance estimation can only be implemented columnwisely, which is time-consuming, and cannot exploit the spatial-contextual information well.

To settle the above exposed problems, we propose an efficient two-phase multiobjective sparse unmixing (Tp-MoSU+) approach by designing more suitable similarity measure in this article. First, we thoroughly analyze the underlying reason for the poor performance of Tp-MoSU in identifying the real endmembers under heavy noise and point out the limitations of F -norm-based residual objective used in the first phase of Tp-MoSU. Then, a CSS measure is established to overcome the limitations. In the second phase, we first analyze the possible reasons for why Tp-MoSU cannot estimate the abundances as a whole and then construct an $L_{2,\infty}$ -norm-based residual objective, which measures the maximum unmixing residuals among all the pixels. We thus optimize this objective and the TV regularizer simultaneously to estimate the abundances. The evolutionary operators are also elaborately redesigned to help reduce the reconstructed objective in order to facilitate the estimation of abundances for all pixels as a whole. The main advantages of Tp-MoSU+ are as follows.

- 1) Tp-MoSU+ constructs a CSS measure to evaluate the unmixing residuals, which considers both the spectral shape and amplitude discrepancy between the original and reconstructed spectra, thus achieving better performance on highly noisy data.
- 2) Tp-MoSU+ facilitates the estimation of abundances as a whole using an $L_{2,\infty}$ -norm-based residual objective and the reconstructed evolutionary operators and thus greatly

reduces the computational complexity and improves the utilization of spatial-contextual information among the adjacent pixels of an image.

The remainder of this article is organized in the following steps. Section II reviews our previous two-phase multiobjective optimization model for sparse unmixing. Section III establishes Tp-MoSU+ gradually based on the quantitative analysis. Section IV introduces the solving algorithm for Tp-MoSU+ model. Section V verifies Tp-MoSU+ using the synthetic as well as real datasets. Section VI concludes this article.

II. MULTIOBJECTIVE OPTIMIZATION FOR SPARSE UNMIXING

In this section, we mainly review the commonly used linear sparse unmixing model and illustrate how the multiobjective optimization serves sparse unmixing tasks.

The LMM with ANC and ASC can be described as

$$\begin{aligned} \mathbf{Y} &= \mathbf{A}\mathbf{X} + \mathbf{N} \\ \text{s.t. } \mathbf{X} &\geq 0, \mathbf{1}_q^T \mathbf{X} = \mathbf{1}_N^T \end{aligned} \quad (1)$$

where $\mathbf{Y}_{L \times N}$ is an observed hyperspectral image with N pixels, each of which has L spectral bands. $\mathbf{A}_{L \times q}$ is a matrix containing q spectral signatures (endmembers), and $\mathbf{X}_{q \times N}$ is the corresponding abundance matrix. \mathbf{N} models the additive noise in the observation process. Note that $\mathbf{X} \geq 0$ should be understood in an elementwise sense.

In sparse unmixing, an overcomplete spectral library is directly assigned to the matrix \mathbf{A} , so the abundance matrix \mathbf{X} should be sparse, which can be induced by the sparse regularizer. In addition, the spatial-contextual information can be exploited by a suitable spatial regularizer. Therefore, sparse unmixing tasks generally optimize

$$\begin{aligned} \min_{\mathbf{X}} \quad & \|\mathbf{Y} - \mathbf{A}\mathbf{X}\|_F + \lambda_1 J_{\text{sps}}(\mathbf{X}) + \lambda_2 J_{\text{spt}}(\mathbf{X}) \\ \text{s.t. } \quad & \mathbf{X} \geq 0, \mathbf{1}_q^T \mathbf{X} = \mathbf{1}_N^T \end{aligned} \quad (2)$$

where λ_1 and λ_2 are two regularization parameters. $J_{\text{sps}}(\mathbf{X})$ denotes the sparse regularizer, and usually, $J_{\text{sps}}(\mathbf{X}) = \|\mathbf{X}\|_{2,1}$ [19]; $J_{\text{spt}}(\mathbf{X})$ denotes the spatial regularizer such as the TV [20] and nonlocal means regularizers [22]. To eliminate the regularization parameter issue, the interplay of regularizers, and the drawback of “decision ahead of solution” behavior, we proposed a Tp-MoSU method in [32] instead of the model (2) within the multiobjective evolutionary algorithm based on decomposition (MOEA/D) framework [33].

Tp-MoSU identifies the real endmembers and estimates their abundances in two successive phases. In the first phase, it identifies the real endmembers with a subset selection problem by minimizing the unmixing residuals and the number of real endmembers as

$$\min_{\mathbf{I}} : \{ \|\mathbf{Y} - \mathbf{A}_I \mathbf{X}_I\|_F, \|\mathbf{I}\|_0 \} \quad (3)$$

where \mathbf{I} is a binary vector whose length equals to the column number of \mathbf{A} , \mathbf{A}_I consists of the columns of \mathbf{A} corresponding to the nonzero elements of \mathbf{I} , and $\mathbf{X}_I = (\mathbf{A}_I^T \mathbf{A}_I)^{-1} \mathbf{A}_I^T \mathbf{Y}$. The

objective $\|\mathbf{I}\|_0$ plays a similar role as the sparse regularizer in (2).

Once the optimal binary vector \mathbf{I}_{opt} is obtained, the real endmembers ($\mathbf{M} = \mathbf{A}_{\mathbf{I}_{\text{opt}}}$) are also determined. In the second phase, Tp-MoSU estimates the abundance vector of the j th pixel (i.e., \mathbf{S}_j) with

$$\min_{\mathbf{S}_j \geq 0} \{ \|\mathbf{Y}_j - \mathbf{M}\mathbf{S}_j\|_2, J_{\text{spt}}(\mathbf{S}_j) \}, \quad j=1, 2, \dots, N. \quad (4)$$

Note that the ASC in (2) is not imposed in this model because the ANC can impose a generalized ASC potentially [10]. Both problems (3) and (4) are decomposed into a series of scalar sub-problems using the Tchebycheff approach within the MOEA/D framework and then solved by the designed evolutionary algorithms. For more details about how the Tp-MoSU model is established and solved, readers are suggested to refer to [33] and [32].

III. TP-MOSU+ MODELING

This section mainly analyzes the limitations of Tp-MoSU and explains our motivation for improving each of the two phases. In the first phase, we first analyze the disability of the F -norm in utilizing the spectral shape features while measuring the spectral similarity and then construct a CSS measure to exploit both the spectral amplitude and shape discrepancy between the original and reconstructed spectra. In the second phase, we first analyze the reasons for the limited efficiency of Tp-MoSU in exploiting the spatial-contextual information and then construct an $L_{2,\infty}$ -norm-based residual objective and redesign the optimization operators to estimate the abundance matrix as a whole, thus better exploiting the spatial-contextual information and reducing the time complexity.

A. Composite Spectral Similarity Measure

Spectral similarity measure is very important in spectral similarity analysis, e.g., spectrum reconstruction and spectral clustering. In Tp-MoSU [32], we simply used the F -norm to evaluate the difference between the original and reconstructed spectra, and the experimental results showed that Tp-MoSU achieved better performance in identifying the real endmembers under slight noise, but limited performance under heavy noise. To better describe the reason, we denote the gain and offset in the spectral amplitude as follows:

$$\mathbf{v}_g = \mathbf{k} \odot \mathbf{v} \quad (5a)$$

$$\mathbf{v}_o = \mathbf{v} + \mathbf{b} \quad (5b)$$

where \mathbf{v} is the original spectral vector, and \mathbf{k} and \mathbf{b} are the gain and offset vectors, respectively. \odot and $+$ denote the elementwise multiplication and addition, respectively.

We now present two examples to illustrate the sensitivity of the F -norm (i.e., the l_2 norm when measuring vectors) to the gain and offset in the spectral amplitude:

1) *Example 1 (\mathbf{k} or \mathbf{b} Is a Constant Vector)*: As shown in Fig. 1(a), assuming that \mathbf{y}_1 is the reference spectral vector, \mathbf{y}_2 and \mathbf{y}_3 are two test spectral vectors such that $\mathbf{y}_3 =$

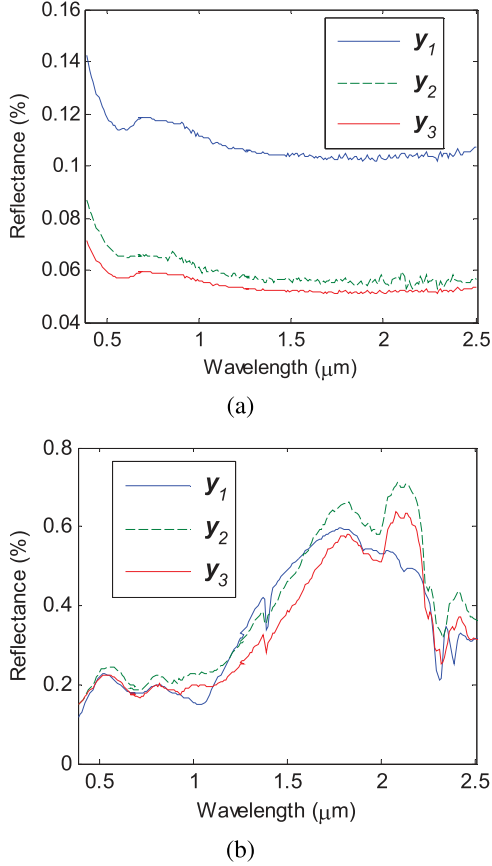


Fig. 1. (a) and (b) Gain and offset effects of the spectral amplitude on the spectral similarity based on l_2 -norm.

TABLE I
 l_2 -NORM AND SAM (RAD) OF $(\mathbf{y}_1, \mathbf{y}_2)$ AND $(\mathbf{y}_1, \mathbf{y}_3)$ BEFORE AND AFTER THE VECTOR NORMALIZATION IN EXAMPLE 1

Example 1	$(\mathbf{y}_1, \mathbf{y}_2)$		$(\mathbf{y}_1, \mathbf{y}_3)$	
	l_2 -norm	SAM	l_2 -norm	SAM
Original	0.7369	0.0374	0.8166	0
Normalized	0.0362	0.0374	0	0

$(0.5, 0.5, \dots, 0.5) \odot \mathbf{y}_1$. Table I presents the l_2 -norm and spectral angle mapper (SAM) of $(\mathbf{y}_1, \mathbf{y}_2)$ and $(\mathbf{y}_1, \mathbf{y}_3)$ before and after the vector normalization. From this table, we can find that the l_2 -norm between the spectral vector \mathbf{y}_1 and \mathbf{y}_3 is obviously larger than that between \mathbf{y}_1 and \mathbf{y}_2 . Therefore, \mathbf{y}_1 is more similar to \mathbf{y}_2 than to \mathbf{y}_3 in terms of the l_2 -norm. However, the vector \mathbf{y}_3 is actually a scaling vector of \mathbf{y}_1 as in the assumption, so \mathbf{y}_1 is more similar to \mathbf{y}_3 than to \mathbf{y}_2 in terms of the SAM, which measures the spectral similarity based on the spectral angle [1], i.e.,

$$\text{SAM}(\mathbf{y}_1, \mathbf{y}_2) = \arccos \frac{\mathbf{y}_1^T \mathbf{y}_2}{\|\mathbf{y}_1\|_2 \|\mathbf{y}_2\|_2} \quad (6)$$

2) *Example 2 (\mathbf{k} and \mathbf{b} Are Nonconstant Vectors)*: As shown in Fig. 1(b), we still assume that \mathbf{y}_1 is the reference spectral vector, \mathbf{y}_2 and \mathbf{y}_3 are two test spectral vectors, but \mathbf{k} and \mathbf{b}

TABLE II
 l_2 -NORM AND SAM (RAD) OF $(\mathbf{y}_1, \mathbf{y}_2)$ AND $(\mathbf{y}_1, \mathbf{y}_3)$ BEFORE AND AFTER THE VECTOR NORMALIZATION IN EXAMPLE 2

Example 2	$(\mathbf{y}_1, \mathbf{y}_2)$		$(\mathbf{y}_1, \mathbf{y}_3)$	
	l_2 -norm	SAM	l_2 -norm	SAM
Original	1.0626	0.1343	0.8635	0.1501
Normalized	0.1339	0.1343	0.1498	0.1501

are no longer constant vectors. Table II presents the l_2 -norm and SAM of $(\mathbf{y}_1, \mathbf{y}_2)$ and $(\mathbf{y}_1, \mathbf{y}_3)$ before and after the vector normalization. From this table, we can find that the l_2 -norm between the spectral vector \mathbf{y}_1 and \mathbf{y}_2 is obviously larger than that between \mathbf{y}_1 and \mathbf{y}_3 . Therefore, \mathbf{y}_1 is more similar to \mathbf{y}_3 than to \mathbf{y}_2 in terms of the l_2 -norm. However, the SAM between the vector \mathbf{y}_1 and \mathbf{y}_3 is larger than that of \mathbf{y}_1 and \mathbf{y}_2 , so \mathbf{y}_1 is more similar to \mathbf{y}_2 than to \mathbf{y}_3 in terms of the SAM.

From the above two examples, we can see that the performance of l_2 -norm in measuring the spectral similarity is easy to be degraded by the gain and offset in the spectral amplitude. The reason lies in that the l_2 -norm purely measures the amplitude difference between spectra and, thus, is oversensitive to the gain and offset in the spectral amplitude [34]. In fact, the information associated with a spectral vector includes both the spectral amplitude and the spectral shape along the spectral bands. Therefore, the F -norm purely accumulating the amplitude difference in terms of the l_2 -norm is incapable of utilizing the shape features to measure spectral similarity.

In order to utilize both the spectral shape and amplitude features in measuring spectral similarity, we need to connect the l_2 -norm with a spectral similarity measure, which is constructed merely based on the spectral shape features. Fortunately, the spectral correlation angle (SCA) [35] happens to hit the spot, which is defined as

$$\text{SCA}(\mathbf{y}_i, \mathbf{y}_j) = \arccos [\rho(\mathbf{y}_i, \mathbf{y}_j)] \quad (7)$$

where \mathbf{y}_i and \mathbf{y}_j are two column vectors, $\text{SCA} \in [0, \pi]$, and $\rho(\cdot, \cdot)$ denotes the Pearson correlation coefficient

$$\rho(\mathbf{y}_i, \mathbf{y}_j) = \frac{\langle \mathbf{y}_i - \bar{y}_i, \mathbf{y}_j - \bar{y}_j \rangle}{\|\mathbf{y}_i - \bar{y}_i\|_2 \|\mathbf{y}_j - \bar{y}_j\|_2} \quad (8)$$

where \bar{y}_i and \bar{y}_j are the mean values of \mathbf{y}_i and \mathbf{y}_j , respectively. Thus, SCA is invariant to the constant gain and offset in the spectral amplitude, i.e.,

$$\text{SCA}(\mathbf{y}_i, \mathbf{y}_j) = \text{SCA}(\mathbf{y}_i, k\mathbf{y}_j + \mathbf{b}), \quad k, b \neq 0 \quad (9)$$

so it mainly calculates the spectral shape differences between two spectra.

To connect the l_2 -norm and SCA, the multiplication rather than addition is used because the addition cannot balance the effects of l_2 -norm and SCA when they have magnitude discrepancy. Therefore, a novel composite spectral similarity measure is constructed as the product of the l_2 -norm and SCA, i.e.,

$$\text{CSS}(\mathbf{Y}, \hat{\mathbf{Y}}) = \sum_{j=1}^N \|\mathbf{Y}_j - \hat{\mathbf{Y}}_j\|_2 \cdot \text{SCA}(\mathbf{Y}_j, \hat{\mathbf{Y}}_j) \quad (10)$$

where \mathbf{Y}_j and $\hat{\mathbf{Y}}_j$ are the j th columns of \mathbf{Y} and $\hat{\mathbf{Y}}$, respectively.

As a result, the first phase of Tp-MoSU+ optimizes

$$\min_{\mathbf{I}} : \{\text{CSS}(\mathbf{Y}, \mathbf{A}_I \mathbf{X}_I), \|\mathbf{I}\|_0\} \quad (11)$$

where the vector \mathbf{I} and the matrices \mathbf{A}_I and \mathbf{X}_I are the same as in (3).

B. $L_{2,\infty}$ -Norm-Based Residual Measure

In the second phase of Tp-MoSU, the model (4) is solved columnwisely (i.e., pixel-by-pixel) because the abundance matrix \mathbf{S} cannot be estimated as a whole by the designed algorithm. Therefore, optimizing the model (4) is a very tedious and time-consuming task, and the spatial-contextual information among adjacent pixels cannot be effectively exploited.

In fact, we have attempted to estimate the whole abundance matrix \mathbf{S} in a single run using the algorithm in Tp-MoSU, but the unmixing residual objective decreased hardly before the individuals converge to the Pareto-optimal set. By analyzing the change of unmixing residuals of each pixel as the individual evolves, we found that there always exist some pixels whose unmixing residuals increase, which obstructs the reduction of the total unmixing residuals. Now, we attempt to analyze the possible reasons for the increase below.

In Algorithm 3 of Tp-MoSU [32], the individuals are evolved with the recombination, mutation, and local search operators as the iteration goes, which may be the reasons for the increase in the unmixing residuals of some pixels. Now, we analyze their effects on the unmixing residuals of pixels, respectively.

1) *Recombination*: If the abundance matrix \mathbf{S} is estimated as a whole, the linear recombination used in Tp-MoSU should be extended to

$$\bar{\mathbf{S}} = \lambda \mathbf{S}^k + (1 - \lambda) \mathbf{S}^l \quad (12)$$

where \mathbf{S}^k and \mathbf{S}^l are two parent individuals, $\bar{\mathbf{S}}$ is the offspring, and λ is the combination coefficient. Denoting $\boldsymbol{\delta} = \mathbf{Y}_j - \mathbf{M}\bar{\mathbf{S}}_j$, $\boldsymbol{\delta}_k = \mathbf{Y}_j - \mathbf{M}\mathbf{S}_j^k$, and $\boldsymbol{\delta}_l = \mathbf{Y}_j - \mathbf{M}\mathbf{S}_j^l$, then the unmixing residuals of the j th pixel corresponding to the offspring $\bar{\mathbf{S}}$ can be calculated as

$$\|\boldsymbol{\delta}\|_2 = \|\lambda \boldsymbol{\delta}_k + (1 - \lambda) \boldsymbol{\delta}_l\|_2. \quad (13)$$

Thus, $\|\boldsymbol{\delta}\|_2$ is not guaranteed to be less than both $\|\boldsymbol{\delta}_k\|_2$ and $\|\boldsymbol{\delta}_l\|_2$. For example, when $\boldsymbol{\delta}_k^T \boldsymbol{\delta}_l \geq \min\{\|\boldsymbol{\delta}_k\|_2^2, \|\boldsymbol{\delta}_l\|_2^2\}$,

$$\begin{aligned} \|\boldsymbol{\delta}\|_2^2 &= \|\lambda \boldsymbol{\delta}_k + (1 - \lambda) \boldsymbol{\delta}_l\|_2^2 \\ &= \lambda^2 \|\boldsymbol{\delta}_k\|_2^2 + (1 - \lambda)^2 \|\boldsymbol{\delta}_l\|_2^2 + 2\lambda(1 - \lambda) \boldsymbol{\delta}_k^T \boldsymbol{\delta}_l \\ &\geq [\lambda^2 + (1 - \lambda)^2 + 2\lambda(1 - \lambda)] \min\{\|\boldsymbol{\delta}_k\|_2^2, \|\boldsymbol{\delta}_l\|_2^2\} \\ &= \min\{\|\boldsymbol{\delta}_k\|_2^2, \|\boldsymbol{\delta}_l\|_2^2\}. \end{aligned} \quad (14)$$

Therefore, the recombination process may be the reason for the increase in the unmixing residuals of some pixels as the individual evolves.

2) *Mutation*: If the abundance matrix \mathbf{S} is estimated as a whole, the Gaussian mutation operator used in Tp-MoSU is

better to be kept invariant, i.e.,

$$p(\mathbf{S}_j \leftarrow \bar{\mathbf{S}}_j) = \frac{1}{\sqrt{2\pi}\sigma} \exp\left(-\frac{(\mathbf{S}_j - \bar{\mathbf{S}}_j)^2}{2\sigma^2}\right) \quad (15)$$

where $j = 1, 2, \dots, N$, and σ is a positive constant controlling the mutation range. This is because different columns of $\bar{\mathbf{S}}$ have different magnitudes, it would be more reasonable to mutate them columnwisely. Obviously, $\|\mathbf{Y}_j - \mathbf{M}\bar{\mathbf{S}}_j\|_2^2$ is not necessarily less than $\|\mathbf{Y}_j - \mathbf{M}\mathbf{S}_j\|_2^2$, so this mutation process may also be the reason for the increase in the unmixing residuals of some pixels as the individual evolves.

3) *Local Search*: If the abundance matrix in the t th iteration, i.e., $\mathbf{S}\{t\}$, is estimated as a whole, the multiplicative update rule used in Tp-MoSU should be extended to

$$\mathbf{S}\{t+1\} = \mathbf{S}\{t\} \odot (\mathbf{M}^T \mathbf{Y}) \oslash (\mathbf{M}^T \mathbf{M} \mathbf{S}\{t\}) \quad (16)$$

where \odot and \oslash denote the elementwise multiplication and division, respectively. In fact, (16) can be written in a gradient descent form columnwisely [36] as

$$\mathbf{S}_j\{t+1\} = \mathbf{S}_j\{t\} + \eta_j [(\mathbf{M}^T \mathbf{Y})_j - (\mathbf{M}^T \mathbf{M} \mathbf{S}\{t\})_j] \quad (17)$$

where $\eta_j = \mathbf{S}_j\{t\} \oslash (\mathbf{M}^T \mathbf{M} \mathbf{S}\{t\})_j$. Therefore, this local search method guarantees to reduce the unmixing residuals of each pixel as the individual evolves.

In summary, both the recombination and mutation processes could be the reasons for why the Tp-MoSU algorithm does not converge when estimating the abundance matrix \mathbf{S} as a whole.

After reviewing the recombination operator (12) and the mutation operator (15), we find that (12) and (15) recombine and mutate all the columns of the parent individuals indiscriminately. This has the potential to reduce the unmixing residuals of some pixels, but may also increase that of the others at the same time, thus leading to the increase of the total unmixing residuals. To solve this problem, we need to reestablish the model and reconstruct the optimization operators to optimize the unmixing residuals for each pixel independently. In addition, to reduce the total unmixing residuals of all the pixels more efficiently, we should focus mainly on the pixels with high unmixing residuals and optimize their abundances without worsening that of the others. However, the F -norm-based objective roughly calculates the total unmixing residuals of all the pixels, so the abundances of the targeted pixels can hardly be optimized independently.

In order to meet the above intention, an $L_{2,\infty}$ -norm-based residual objective is established as

$$\text{OBJ2} = \|\mathbf{Y} - \mathbf{M}\mathbf{S}\|_{2,\infty} \quad (18)$$

where $\|\mathbf{C}\|_{2,\infty} = \max\{\|\mathbf{C}(:,j)\|_2, j=1, 2, \dots, N\}$. This objective measures the maximum unmixing residuals among all the pixels, so it is targeted on the pixel, which ranks the first in occupying the unmixing residuals. In addition, the unmixing residuals of each pixel can be obtained while calculating (18). Therefore, this objective is more conducive to optimizing the unmixing residuals of each pixel independently. Finally, by

reducing the objective $OBJ2$ without increasing the unmixing residuals of the other pixels, the total unmixing residuals $\|\mathbf{Y} - \mathbf{M}\mathbf{S}\|_F$ can be reduced collaboratively.

As a result, the second phase of Tp-MoSU+ optimizes

$$\min_{\mathbf{S} \geq 0} : \{OBJ2, J_{\text{spt}}(\mathbf{S})\}. \quad (19)$$

Based on the above analysis, in order to reduce the unmixing residuals of all the pixels collaboratively, we need to redesign the optimization operators to match the new objective (18) in the following section.

IV. ALGORITHMS FOR TP-MOSU+

Although the objective in each phase of Tp-MoSU+ has been reestablished, the algorithmic framework for Tp-MoSU can still be used to optimize Tp-MoSU+ because of its extensibility. In the following, we analyze whether the optimization operators in the algorithmic framework should be redesigned or not.

In the first phase, the only difference between Tp-MoSU and Tp-MoSU+ is the unmixing residual objective, so the endmember selection algorithm designed for Tp-MoSU in [32] can be directly used for Tp-MoSU+. Therefore, in order to highlight the strength of the CSS measure as compared with the F -norm, we do not make any change to the optimization algorithm to avoid unpredictable effects. In addition, among all the Pareto optimal solutions obtained by the endmember selection algorithm, the knee point search strategy [37] is still used to decide the final solution because this solution generally corresponds to the real endmembers as proved in [32].

In the second phase, we need to redesign the optimization operators within [32, Algorithm 3] for Tp-MoSU+ to match the constructed objective (18). The details are as follows.

1) *Initialization*: Because the real endmembers (\mathbf{M}) have been identified, the initial population for the abundance matrix \mathbf{S} is partly generated randomly to create population diversity and partly configured the same as [32, Algorithm 1] to approach the convergence region.

2) *Evaluation*: Each individual \mathbf{S}^i ($i = 1, 2, \dots, \text{popsize.}$) in the current population is evaluated using the objective (19), and the unmixing residuals of each pixel corresponding to the i th individual \mathbf{S}^i are stored in \mathcal{G}_i for later use

$$\mathcal{G}_i = \{g_j^i | g_j^i = \|\mathbf{Y}_j - \mathbf{M}\mathbf{S}_j^i\|_2, j = 1, 2, \dots, N\} \quad (20)$$

where \mathbf{S}_j^i denotes the j th column of \mathbf{S}^i , and g_j^i denotes its unmixing residuals.

3) *Recombination*: Assuming that \mathbf{S}^k and \mathbf{S}^l ($\mathbf{S}^k \neq \mathbf{S}^l$) are parent individuals to two different neighbors of the i th subproblem, respectively, in order to inherit good genes from both of the two parents, the offspring $\bar{\mathbf{S}}^i$ is generated as

$$\bar{\mathbf{S}}_j^i = \begin{cases} \mathbf{S}_j^k, & g_j^k \leq g_j^l, \\ \mathbf{S}_j^l, & \text{otherwise} \end{cases} \quad j = 1, 2, \dots, N \quad (21)$$

and thus the unmixing residuals of each pixel corresponding to $\bar{\mathbf{S}}^i$ are also inherited from the parents as

$$\bar{\mathcal{G}}_i = \{\bar{g}_j^i | \bar{g}_j^i = \min\{g_j^k, g_j^l\}, j = 1, 2, \dots, N.\} \quad (22)$$

Therefore, this offspring $\bar{\mathbf{S}}^i$ is guaranteed to be better than both of the parents \mathbf{S}^k and \mathbf{S}^l in terms of the unmixing accuracy.

4) *Mutation*: In order to reduce the residual objective (18) efficiently, we select the abundance vector with probability proportional to its unmixing residuals such that the abundance vector with larger unmixing residuals can be mutated with a larger probability. Therefore, based on the unmixing residuals (22) of all pixels, the j th ($j = 1, 2, \dots, N.$) column of the offspring $\bar{\mathbf{S}}^i$ is selected using the roulette wheel selection [38] with probability

$$p_j = \frac{\|\mathbf{Y}_j - \mathbf{M}\bar{\mathbf{S}}_j^i\|_2}{\sum_{j=1}^N \|\mathbf{Y}_j - \mathbf{M}\bar{\mathbf{S}}_j^i\|_2} \quad (23)$$

and then mutated to \mathbf{S}^i with probability (15).

5) *Local Search*: Because improving the abundance matrix \mathbf{S} using (16) guarantees to reduce the unmixing residuals of each pixel, the multiplicative update rule (16) is still used as the local search method.

With the above redesigned evolutionary operators, we can optimize the objective (19) within [32, Algorithm 3] and obtain a set of Pareto optimal solutions in a single run. In this way, the computational complexity for estimating the abundance matrix can be greatly reduced, and the spatial-contextual information among adjacent pixels can be better utilized. In addition, among all the obtained Pareto optimal solutions, the one with the least unmixing residuals is selected as the final abundance matrix because accuracy is the primary goal of unmixing tasks.

V. EXPERIMENTAL STUDIES

In this section, the proposed Tp-MoSU+ is tested in three steps. First, the capability of the first phase in identifying the real endmembers is investigated with the synthetic data because the ground-truth information is available to verify the proposed method quantitatively. Second, the capability of the second phase in estimating the abundances is tested with two representative and two challenging synthetic datasets. Finally, the proposed Tp-MoSU+ is used to unmix a real hyperspectral image in compare with some state-of-the-art unmixing methods. In summary, these three steps can provide valuable insight into the overall effectiveness of the proposed Tp-MoSU+ for HU.

The parameters in the two phases of Tp-MoSU+ and Tp-MoSU are set identically. Specifically, the population size, the maximum iteration number, and the crossover probability in the two phases are set equally to 100, 200, and 1, respectively. The neighbor sizes in the two phases are set to 15 and 10, respectively. The mutation probabilities in the two phases are set to $1/q$ and $1/k$, respectively, where q is the size of the spectral library, and k is the number of the estimated endmembers in the first phase. The parameter σ in the second phase is set to one-thirtieth magnitude of each individual. To ensure the reliability, the experiments are repeated for 20 times, and their average results are presented.

A. Experiments on the First Phase of Tp-MoSU+

Because Tp-MoSU+ is established within the two-phase multiobjective optimization sparse unmixing framework, and the

TABLE III

RESULTS OF Tp-MoSU+ IN IDENTIFYING VARYING NUMBER OF REAL ENDMEMBERS UNDER VARYING NOISE LEVELS AS COMPARED WITH Tp-MoSU BASED ON THE LIBRARY \mathcal{A}_1 (THE VALUES IN THE FIRST/SECOND COLUMN BELOW EACH INDICATOR ARE OBTAINED BY Tp-MoSU+/Tp-MoSU)

Tp-MoSU+/Tp-MoSU																				
p	5				8				10				12				15			
	SNR	AN		CER		AN		CER		AN		CER		AN		CER		AN		CER
5	2.1	1.8	0.00	0.00	2.2	1.5	0.00	0.00	1.5	1.0	0.00	0.00	1.3	1.1	0.00	0.00	1.5	1.4	0.00	0.00
10	3.9	3.6	0.30	0.10	3.8	3.5	0.00	0.00	4.4	3.9	0.00	0.00	3.7	3.1	0.00	0.00	4.1	3.7	0.00	0.00
15	4.2	3.9	0.50	0.20	4.8	4.6	0.00	0.00	4.6	4.1	0.00	0.00	6.1	4.4	0.00	0.00	5.0	4.3	0.00	0.00
20	4.3	3.8	0.50	0.20	5.9	5.8	0.00	0.00	7.1	6.3	0.00	0.00	7.2	6.5	0.00	0.00	6.2	5.9	0.00	0.00

TABLE IV

RESULTS OF Tp-MoSU+ IN IDENTIFYING VARYING NUMBER OF REAL ENDMEMBERS UNDER VARYING NOISE LEVELS AS COMPARED WITH Tp-MoSU BASED ON THE LIBRARY \mathcal{A}_2

Tp-MoSU+/Tp-MoSU																				
p	5				8				10				12				15			
	SNR	AN		CER		AN		CER		AN		CER		AN		CER		AN		CER
5	3.5	2.0	0.30	0.00	3.0	2.3	0.00	0.00	3.7	2.9	0.00	0.00	3.8	1.6	0.00	0.00	3.9	2.1	0.00	0.00
10	4.6	3.4	0.70	0.10	5.5	5.0	0.00	0.00	5.7	5.6	0.00	0.00	4.3	3.4	0.00	0.00	5.0	3.3	0.00	0.00
15	4.7	4.4	0.70	0.60	6.4	6.0	0.20	0.00	8.1	7.8	0.20	0.00	6.9	6.6	0.00	0.00	7.5	5.7	0.00	0.00
20	4.9	4.9	0.90	0.90	7.9	7.9	0.90	0.90	8.2	7.9	0.20	0.00	8.5	8.3	0.10	0.00	10.7	10.5	0.00	0.00

CSS measure in the first phase of Tp-MoSU+ is constructed on the basis of analyzing the limitations of Tp-MoSU under heavy noise, Tp-MoSU is used as a comparison to verify the effectiveness of CSS measure in this experiment.

The synthetic data used in this experiments are generated based on the LMM (1) using the endmembers chosen from the USGS digital spectral library—splib06.¹ In order to study the performance of the CSS measure under spectral signatures with different mutual coherence (i.e., correlation), three libraries \mathcal{A}_1 , \mathcal{A}_2 , and \mathcal{A}_3 are obtained by pruning the USGS library with the spectral angle distance of 0° , 3° and 5° , respectively, and thus, their mutual coherence is decreasing, namely, the correlation between spectral signatures of the library is decreasing. Then, the synthetic data with 1000 pixels are generated using the endmembers chosen from the library \mathcal{A}_1 , \mathcal{A}_2 , and \mathcal{A}_3 , respectively. In order to study the performance of the CSS measure under heavy additive noise, the Gaussian white noise with varying SNR ($\text{SNR} \equiv 10\log_{10}(\|\mathbf{A}\mathbf{X}\|_2^2/\|\mathbf{N}\|_2^2)$) from 5 to 20 with a step size of 5 is imposed on each synthetic data, respectively. To quantify the performance of the constructed CSS measure of Tp-MoSU+ in identifying the real endmembers, the correct estimation rate (CER) and the average number (AN) of accurately estimated endmembers defined in [32] are used as two indicators. Specifically,

$$\text{CER} = \text{NC}/\text{NT} \quad (24)$$

and

$$\text{AN} = \frac{\sum_{n=1}^{\text{NT}} N_n}{\text{NT}} \quad (25)$$

where NC is the frequency of the correct identification of all the real endmembers, NT is the total number of trials, and N_n is the number of accurately identified real endmembers in the n th trial.

The results of Tp-MoSU+ in identifying varying number of real endmembers (denoted as p) under varying noise levels as compared with Tp-MoSU based on the library \mathcal{A}_1 , \mathcal{A}_2 , and \mathcal{A}_3

are listed in Tables III–V, respectively. Based on these results, we analyze the performance of Tp-MoSU+ against the varying number of real endmembers, the varying noise level, and the varying mutual coherence of spectral library, respectively, as follows.

1) *Varying Number of Real Endmembers*: The AN and CER values obtained by Tp-MoSU+ and Tp-MoSU in identifying varying number of real endmembers under fixed SNR and fixed spectral library are listed in each row of Tables III–V. From these three tables, we find that almost all the AN values obtained by Tp-MoSU+ are larger than that obtained by Tp-MoSU under the same noise level and the same spectral library. Besides, the CER value obtained by Tp-MoSU+ is generally larger than that obtained by Tp-MoSU under the same noise level and the same spectral library unless they are all equal to zero. This verifies that Tp-MoSU+ outperforms Tp-MoSU in identifying varying number of real endmembers under the same noise level and the same spectral library.

Furthermore, the AN value increases quite slow and sometimes even decreases with the increasing number of real endmembers especially when the SNR has low value, and the spectral library has high mutual coherence. For example, when the number of real endmembers increases, the AN value in the first row of Table III decreases in general, while that in the bottom row of Table V increases significantly. In addition, the CER values in the lower left corner of each table are larger than the values elsewhere, and the CER values in Table V are larger than that in Table III correspondingly. This discloses that the proposed Tp-MoSU+ has increasing difficulty in identifying all the real endmembers when their number increases, and this situation is increasingly severe with the increasing noise level and increasing mutual coherence of the spectral library.

2) *Varying Noise Level*: The AN and CER values obtained by Tp-MoSU+ and Tp-MoSU in identifying the same number of real endmembers under different noise levels are listed in each column of Tables III–V. From each of these three tables, we find

¹[Online]. Available: <http://speclab.cr.usgs.gov/spectral.lib06>

TABLE V
RESULTS OF Tp-MoSU+ IN IDENTIFYING VARYING NUMBER OF REAL ENDMEMBERS UNDER VARYING NOISE LEVELS AS COMPARED WITH Tp-MoSU BASED ON THE LIBRARY \mathbf{A}_3

Tp-MoSU+/Tp-MoSU																				
p	5				8				10				12				15			
SNR	AN		CER		AN		CER		AN		CER		AN		CER		AN		CER	
5	4.1	4.0	0.10	0.00	5.4	4.9	0.00	0.00	5.3	5.0	0.00	0.00	5.3	5.3	0.00	0.00	5.8	5.7	0.00	0.00
10	4.5	4.3	0.50	0.40	6.4	5.1	0.30	0.00	6.3	6.3	0.00	0.00	7.7	7.6	0.00	0.00	8.8	8.6	0.00	0.00
15	4.8	4.8	0.90	0.80	6.6	5.6	0.30	0.00	7.3	7.1	0.10	0.00	9.1	9.1	0.00	0.00	10.2	9.9	0.00	0.00
20	5.0	4.7	1.00	0.70	7.3	6.4	0.50	0.00	8.0	7.4	0.20	0.00	10.0	8.8	0.10	0.00	11.4	10.6	0.00	0.00

that almost all the AN values obtained by Tp-MoSU+ are larger than that obtained by Tp-MoSU for the same number of real endmembers under the same noise level, and the corresponding CER values obtained by Tp-MoSU+ are generally larger than that obtained by Tp-MoSU unless they are all equal to zero. This verifies that Tp-MoSU+ outperforms Tp-MoSU in identifying the same number of real endmembers based on the same spectral library when the noise level changes.

Furthermore, the AN value obtained by Tp-MoSU+ increases in identifying the same number of real endmembers when the SNR increases, i.e., the noise level decreases. In addition, the CER value obtained by Tp-MoSU+ also increases in identifying the same number of real endmembers when the SNR increases unless it is always equal to zero. This reveals that the proposed Tp-MoSU+ can identify the real endmembers more easily when the noise level decreases.

3) *Varying Mutual Coherence of Spectral Library*: The AN and CER values obtained by the proposed Tp-MoSU+ in identifying real endmembers under the spectral library \mathbf{A}_1 , \mathbf{A}_2 , and \mathbf{A}_3 are listed in Tables III–V, respectively. From these tables, we find that the AN value obtained by Tp-MoSU+ in identifying the same number of real endmembers under the same noise level increases when the spectral library changes from \mathbf{A}_1 to \mathbf{A}_2 , and \mathbf{A}_2 to \mathbf{A}_3 . In addition, the corresponding CER value obtained by Tp-MoSU+ also increases when the spectral library changes from \mathbf{A}_1 to \mathbf{A}_2 , and \mathbf{A}_2 to \mathbf{A}_3 unless it is always equal to zero. Furthermore, the proposed Tp-MoSU+ can rarely identify all the real endmembers based on the library \mathbf{A}_1 (as shown by the few number of nonzero values of CER in Table III), but it can achieve more success in identifying all the real endmembers based on the library \mathbf{A}_3 (as shown by the relatively large number of nonzero values of CER in Table V). All these findings suggest that the performance of Tp-MoSU+ in identifying real endmembers will be degraded by the increasing mutual coherence of the spectral library.

4) *Brief Summary*: Tp-MoSU+ generally outperforms Tp-MoSU in identifying the varying number of real endmembers under different heavy noise based on the spectral library with different mutual coherence, which verifies the effectiveness of the CSS measure in fusing the spectral shape and amplitude features to measure spectral similarity.

B. Experiments on the Second Phase of Tp-MoSU+

This subsection mainly investigates the performance of the second phase of Tp-MoSU+ in estimating the abundances for the identified endmembers in the first phase. In order to provide quantitative as well as qualitative analysis, four advanced

regularization methods, including SUnSAL-TV [20], RS-FoBa [39], SUnSPI [40], MUSIC-CSR [41], and CSUnL0 [29] together with Tp-MoSU [32], are used for comparison. Specifically, SUnSAL-TV is a representative in exploiting similar components among the adjacent pixels; RSFoBa is a representative greedy approach; SUnSPI is a representative in using prior spectral signatures; MUSIC-CSR is a representative collaborative sparse unmixing approach; CSUnL0 is a representative collaborative sparse-inducing approach; Tp-MoSU is a state-of-the-art multiobjective optimization approach which performs well in identifying real endmembers and estimating abundances. Therefore, these approaches are able to investigate the capability of Tp-MoSU+ in different aspects. In order to verify the effect of the local search operator, the Tp-MoSU+ excluding the local search [termed as Tp-MoSU+(N)] is also executed for comparison. In order to provide convincing comparison, the regularization parameters in these four regularization approaches are carefully tuned to a good state. The frequently used signal-to-reconstruction error ($SRE = 20 \log_{10}(E[\|\mathbf{S}\|_2]/E[\|\mathbf{S} - \hat{\mathbf{S}}\|_2])$, where $\hat{\mathbf{S}}$ is the estimated abundances) is used to evaluate the quality of estimated abundances because it can provide the relative intensity of the abundance to its reconstruction error [10].

1) *Experiments on Synthetic Data 1*: The first synthetic data is an image with 75×75 pixels and each of the pixel has 224 spectral bands. These data are generated based on the LMM according to the method provided in [42], which uses five endmembers randomly selected from a sublibrary with 240 spectral signatures of the USGS and five well-designed patch-based abundance matrices as shown in Fig. 2(b)–(f). The background regions in the five abundance matrices have the abundance value of 0.1149, 0.0741, 0.2003, 0.2055, and 0.4051, respectively. As illustrated in Fig. 2(a), the numbers below each patch specify the component endmembers, so the patches in each band of the image include both pure and mixed endmembers ranging from 2 to 5. Therefore, synthetic data 1 is suitable to study the capability of Tp-MoSU+ comprehensively.

In order to study the capability of Tp-MoSU+ in estimating the abundances under different noise interference, the Gaussian white noise of different levels, i.e., SNR = 20, 30, 40, 50, respectively, is imposed on synthetic data 1. The estimated abundances for the noisy data obtained by different algorithms are partly presented in Fig. 3, the average SRE values obtained by these algorithms under different noise levels are listed in Table VI, and the regularization parameter settings in the four regularization methods are also presented in the table.

Fig. 3 presents the abundances of the first and fifth endmembers obtained by different algorithms for the noisy data with

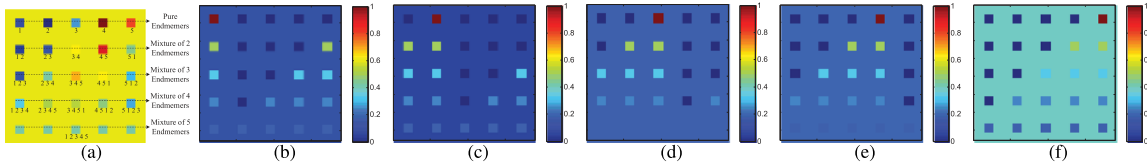


Fig. 2. True fractional abundances of synthetic data 1. (a) 25th band of the simulated image. (b) Abundance 1. (c) Abundance 2. (d) Abundance 3. (e) Abundance 4. (f) Abundance 5.

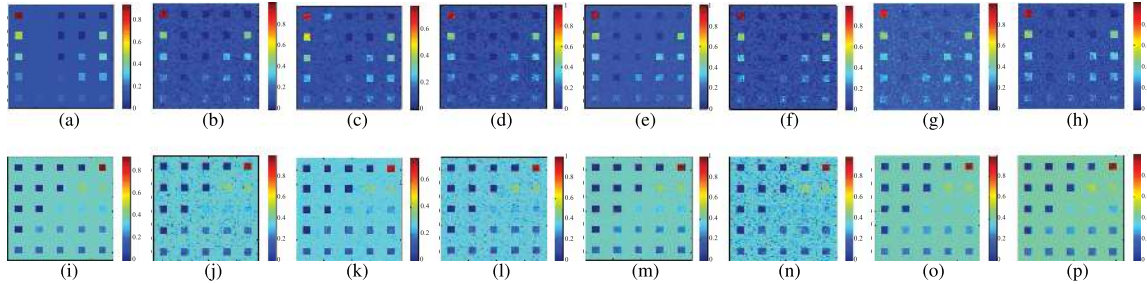


Fig. 3. Estimated abundances of the endmembers (Top row) 1 and (Bottom row) 5 for the noisy data 1 (SNR = 30) obtained by different algorithms. (a) and (i) SUnSAL-TV. (b) and (j) RSFoBa. (c) and (k) SUnSPI. (d) and (l) MUSIC-CSR. (e) and (m) Tp-MoSU. (f) and (n) CSUnL0. (g) and (o) Tp-MoSU+(N). (h) and (p) Tp-MoSU+.

TABLE VI
SRE OF THE PROPOSED Tp-MoSU+ AGAINST THE COMPARISON ALGORITHMS ON THE SYNTHETIC DATA 1 WITH DIFFERENT NOISE LEVELS

SNR	SUnSAL-TV	RSFoBa	SUnSPI	MUSIC-CSR	Tp-MoSU	CSUnL0	Tp-MoSU+(N)	Tp-MoSU+
20	6.1776 ($\lambda = 5e - 4, \lambda_{TV} = 0.05$)	8.1903 ($\lambda = 1$)	5.8087 ($\lambda_S = 0.1, \lambda_P = 3$)	7.0026 ($\lambda_C = 0.5$)	9.6528	7.0102 ($\lambda = 0.001$)	7.4535	9.7089
30	10.5775 ($\lambda = 5e - 4, \lambda_{TV} = 0.01$)	16.8365 ($\lambda = 0.1$)	11.2831 ($\lambda_S = 0.01, \lambda_P = 0.5$)	16.8652 ($\lambda_C = 0.1$)	17.9897	15.9134 ($\lambda = 0.001$)	17.4535	18.1281
40	20.8337 ($\lambda = 5e - 4, \lambda_{TV} = 0.005$)	25.1531 ($\lambda = 0.05$)	18.1390 ($\lambda_S = 0.001, \lambda_P = 0.1$)	25.6674 ($\lambda_C = 0.05$)	26.7892	24.1816 ($\lambda = 0.001$)	25.4931	26.7077
50	30.4471 ($\lambda = 5e - 4, \lambda_{TV} = 0.001$)	33.1405 ($\lambda = 0.01$)	29.1472 ($\lambda_S = 0.001, \lambda_P = 0.05$)	32.4561 ($\lambda_C = 0.01$)	36.4746	31.4758 ($\lambda = 0.001$)	34.4535	35.6113

SNR = 30. It can be seen from Fig. 3(a)–(p) that the abundances obtained by RSFoBa, SUnSPI, MUSIC-CSR, CSUnL0, and Tp-MoSU+(N) contain much more noise than that obtained by SUnSAL-TV, Tp-MoSU, and Tp-MoSU+. Among the latter three algorithms, the abundances obtained by SUnSAL-TV are more smooth than that obtained by Tp-MoSU and Tp-MoSU+, but some patches in the abundances are missing due to the TV regularizer [e.g., see Fig. 3(a)]. By comparing the abundances obtained by Tp-MoSU and Tp-MoSU+, we find that the abundances of the first endmember obtained by Tp-MoSU contain less noise than that obtained by Tp-MoSU+, but the abundances of the fifth endmember obtained by Tp-MoSU contain much more noise than that obtained by Tp-MoSU+. This reveals that Tp-MoSU+ can obtain visually comparable abundances to Tp-MoSU.

From the SRE values presented in Table VI, we find that the SRE values obtained by SUnSAL-TV and SUnSPI are comparable under different noise levels; the SRE values obtained by RSFoBa, MUSIC-CSR, CSUnL0, and Tp-MoSU+(N) are comparable under different noise levels, which are larger than those obtained by SUnSAL-TV and SUnSPI under the same noise level, but the SRE values obtained by Tp-MoSU+ and Tp-MoSU are larger than those obtained by the above

five methods, which reveals that the abundances obtained by Tp-MoSU+ and Tp-MoSU are of the highest quality, and the local search operator is effective in helping Tp-MoSU+ converge quickly. In addition, the SRE values obtained by Tp-MoSU+ are larger than those obtained by Tp-MoSU under heavy noise, i.e., SNR = 20, 30, but smaller under mild noise, i.e., SNR = 40, 50. The reason may lie in that Tp-MoSU estimates abundances columnwisely, while Tp-MoSU+ estimates abundances as a whole, which is able to exploit more spatial-contextual information among adjacent pixels. This helps a lot in improving the abundance quality under heavy noise. However, under mild noise, Tp-MoSU achieves better performance than Tp-MoSU+ because estimating abundances pixel-by-pixel is beneficial for the algorithm to converge better.

Considering the qualitative as well as quantitative results, our proposed Tp-MoSU+ achieves better performance in estimating abundances than the regularization algorithms under different noise levels. It also obtains slightly better performance than Tp-MoSU in estimating abundances under heavy noise, but obtains slightly worse performance under mild noise.

2) *Experiments on Synthetic Data 2*: Synthetic data 2 is an image containing 100×100 pixels and each pixel has 224 spectral bands. These data are generated based on the LMM

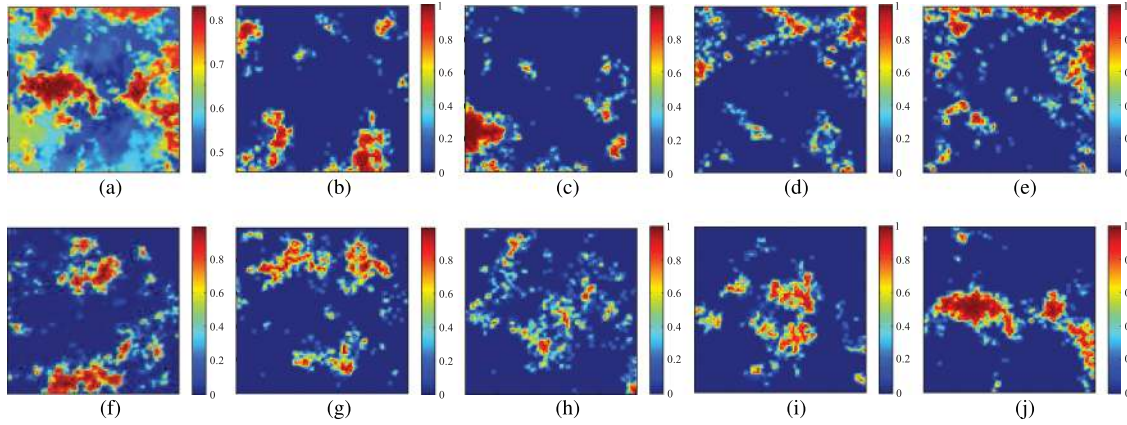


Fig. 4. True fractional abundances of synthetic data 2. (a) One band of the simulated image. (b) True abundance 1. (c) True abundance 2. (d) True abundance 3. (e) True abundance 4. (f) True abundance 5. (g) True abundance 6. (h) True abundance 7. (i) True abundance 8. (j) True abundance 9.

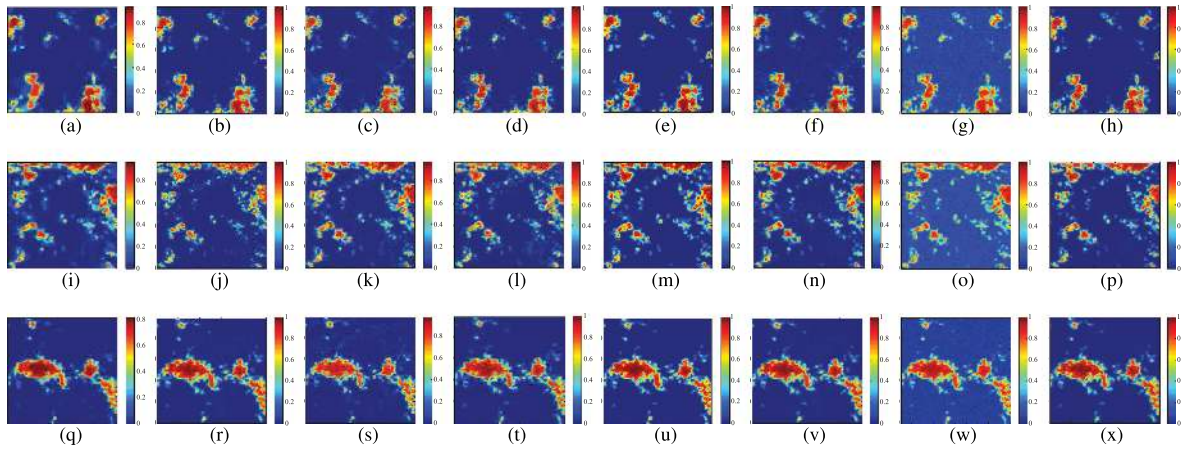


Fig. 5. Estimated abundances of the endmembers (top row) 1, (middle row) 4, and (bottom row) 9 for the noisy data 2 (SNR = 30) obtained by different algorithms. (a), (i), and (q) SUnSAL-TV. (b), (j), and (r) RSFoBa. (c), (k), and (s) SUnSPI. (d), (l), and (t) MUSIC-CSR. (e), (m), and (u) Tp-MoSU. (f), (n), and (v) CSUnL0. (g), (o) and (w) Tp-MoSU+(N). (h), (p), and (x) Tp-MoSU+.

TABLE VII

SRE OF THE PROPOSED Tp-MoSU+ AGAINST THE COMPARISON ALGORITHMS ON THE SYNTHETIC DATA 2 WITH DIFFERENT NOISE LEVELS

SNR	SUnSAL-TV	RSFoBa	SUnSPI	MUSIC-CSR	Tp-MoSU	CSUnL0	Tp-MoSU+(N)	Tp-MoSU+
20	4.8159 ($\lambda = 5e - 4, \lambda_{TV} = 0.05$)	5.1694 ($\lambda = 1$)	4.8567 ($\lambda_S = 0.1, \lambda_P = 3$)	7.7811 ($\lambda_C = 0.5$)	8.4215 -	4.9651 ($\lambda = 5e - 4$)	4.6458 -	8.6258 -
30	9.8007 ($\lambda = 5e - 4, \lambda_{TV} = 0.005$)	11.6294 ($\lambda = 0.5$)	9.6403 ($\lambda_S = 0.01, \lambda_P = 0.1$)	12.6578 ($\lambda_C = 0.05$)	14.4153 -	10.0213 ($\lambda = 5e - 4$)	9.0061 -	16.7830 -
40	17.9802 ($\lambda = 0.005, \lambda_{TV} = 5e - 4$)	18.2207 ($\lambda = 0.1$)	17.3251 ($\lambda_S = 0.005, \lambda_P = 0.05$)	17.3658 ($\lambda_C = 0.05$)	22.5439 -	16.9851 ($\lambda = 5e - 4$)	17.2915 -	22.3615 -
50	23.8434 ($\lambda = 0.001, \lambda_{TV} = 5e - 4$)	26.3186 ($\lambda = 0.05$)	25.4293 ($\lambda_S = 0.001, \lambda_P = 0.01$)	25.6405 ($\lambda_C = 0.05$)	32.5310 -	24.8532 ($\lambda = 5e - 4$)	27.3946 -	31.1217 -

according to the method provided in [20] and [42], which uses nine endmembers randomly selected from a sublibrary with 240 endmembers of the USGS library. The abundances of these endmembers follow a Dirichlet distribution uniformly over the probability simplex [14]. The abundances shown in Fig. 4 exhibit various spatial features, which are suitable for investigating the capability of the spatial similarity exploiting objective (i.e., the TV regularizer) in the proposed Tp-MoSU+.

In order to study the capability of Tp-MoSU+ in estimating the abundances under different noise interference, the Gaussian white noise with SNR = 20, 30, 40, 50, respectively, is imposed on the synthetic data 2. The estimated abundances for the noisy data obtained by different algorithms are partly presented in Fig. 5, the SRE values obtained by these algorithms are presented in Table VII, and the regularization parameter settings in the four regularization methods are also listed in the table.

TABLE VIII
SRE VALUES OBTAINED BY Tp-MoSU+ UNDER DIFFERENT PROPORTIONS OF OUTLIERS AND VARYING NUMBER OF ENDMEMBERS (SNR = 40 dB)

SRE	Proportion of outliers										
	0	0.01	0.02	0.03	0.04	0.05	0.06	0.07	0.08	0.09	0.1
4	37.719	37.737	37.656	37.776	37.721	37.717	37.717	37.708	37.678	37.727	37.729
6	32.562	31.929	32.407	31.862	32.853	32.426	32.786	32.260	32.091	32.491	31.817
8	26.988	26.918	26.937	26.949	26.886	26.965	26.892	26.942	26.919	26.898	26.866
10	21.328	21.303	21.287	21.227	21.278	21.237	21.279	21.217	21.156	21.187	21.203
12	16.813	16.830	16.822	16.747	16.809	16.794	16.739	16.741	16.707	16.725	16.733

Fig. 5 presents the abundances of the first, fourth, and ninth endmembers obtained by different algorithms for the noisy data with SNR = 30. It can be seen from Fig. 5(a)–(x) that the abundances obtained by RSFoBa, SUnSPI, MUSIC-CSR, CSUnL0, and Tp-MoSU+(N) contain too much noise in their blue background regions [e.g., see Fig. 5(j)–(l) and (n)–(o)] than that obtained by SUnSAL-TV, Tp-MoSU, and Tp-MoSU+. Among the latter three algorithms, the abundances obtained by SUnSAL-TV are too smooth so that some little patches are lost and a lot of edges are degraded and indistinct as compared with the true abundances [e.g., see Fig. 5(i) and (q)]. The abundances obtained by Tp-MoSU+ and Tp-MoSU are similar and almost the same as the true abundances visually. Therefore, Tp-MoSU+ can achieve comparable performance to Tp-MoSU in estimating abundances, which is better than the other four regularization algorithms.

From the SRE values presented in Table VII, we find that the SRE values obtained by SUnSAL-TV and SUnSPI are comparable under different noise levels, the SRE values obtained by RSFoBa, CSUnL0, and MUSIC-CSR are comparable under different noise levels, which are larger than that obtained by SUnSAL-TV and SUnSPI under the same noise level, while the SRE values obtained by Tp-MoSU+ and Tp-MoSU are larger than that obtained by these four regularization methods, which means that the abundances obtained by Tp-MoSU+ and Tp-MoSU are of the highest quality. The SRE values obtained by Tp-MoSU+(N) are far less than that obtained by Tp-MoSU+, which verifies the effectiveness of the local search operator (16). In addition, the SRE values obtained by Tp-MoSU+ are larger than that obtained by Tp-MoSU under heavy noise, i.e., SNR = 20, 30, while smaller under mild noise, i.e., SNR = 40, 50. These observations are similar to that obtained on the synthetic data 1 based on the SRE values, so the reasons explained previously are still effective.

Considering the qualitative as well as quantitative results, our proposed Tp-MoSU+ achieves better performance in estimating abundances than the regularization algorithms under different noise levels. It can also obtain slightly better performance than Tp-MoSU in estimating abundances under heavy noise, but obtains slightly worse performance under mild noise.

3) *Robustness to the Outliers and Mismatches*: Since the $L_{2,\infty}$ -norm-based residual objective in the second phase of Tp-MoSU+ measures the maximum unmixing residuals among all the pixels, it may be susceptible to outliers and mismatches between hyperspectral data and the spectral library. In this subsection, we mainly investigate the effects of these two points on the performance of Tp-MoSU+ when estimating abundances. To investigate the negative effects of outliers, we generate the

TABLE IX
SRE VALUES OBTAINED BY Tp-MoSU+ AND Tp-MoSU WHEN THERE EXIST MISMATCHES BETWEEN HYPERSPECTRAL DATA AND THE SPECTRAL LIBRARY (SNR = 40 dB)

SRE	p				
	4	6	8	10	12
Tp-MoSU	35.301	30.053	24.586	20.295	14.852
Tp-MoSU+	35.254	30.721	24.355	20.374	14.627

hyperspectral data containing different proportions of outliers using varying number of endmembers. The SRE values obtained by Tp-MoSU+ are presented in Table VIII. From this table, it can be found that the SRE value obtained by Tp-MoSU+ under the fixed number of endmembers changes slightly as the proportion of outliers increases from 0% to 10%. This reveals that a few outliers in hyperspectral data make little difference to the performance of Tp-MoSU+ when estimating abundances.

To investigate the negative effects of mismatches, we generate the hyperspectral data containing a few pixels whose endmembers are not fully presented in the spectral library. The SRE values obtained by Tp-MoSU+ are presented in Table IX. From this table, it can be found that the SRE values obtained by Tp-MoSU+ are generally smaller than that obtained without outliers and mismatches under the same number of endmembers (as presented in the third column of Table VIII). This reveals that mismatches between hyperspectral data and the spectral library will downgrade the performance of Tp-MoSU+. However, by comparing the SRE values obtained by Tp-MoSU+ and Tp-MoSU under the same condition, it can be found that the performance of Tp-MoSU+ is not worse than Tp-MoSU when estimating abundances. This reveals that the $L_{2,\infty}$ -norm-based residual objective together with the redesigned operators is not necessarily sensitive to the mismatches. Although the performance of Tp-MoSU+ is inevitably downgraded by the mismatches, that is the limitation of all spectral-library-based approaches.

From the above analysis, it can be concluded that Tp-MoSU+ is relatively robust to the outliers and mismatches between hyperspectral data and the spectral library. The reasons may be as follows. First, although the $L_{2,\infty}$ -norm-based residual objective is susceptible to outliers and mismatches, and the redesigned mutation operator optimizes their abundances with higher probability, the abundances of the other pixels also have certain probability to search their best because of the roulette wheel selection method. Second, the recombination operator optimizes the abundances of each pixel independently and ensures the inheritance of the best abundances found for each pixel so far. Third, the local search operator guarantees to

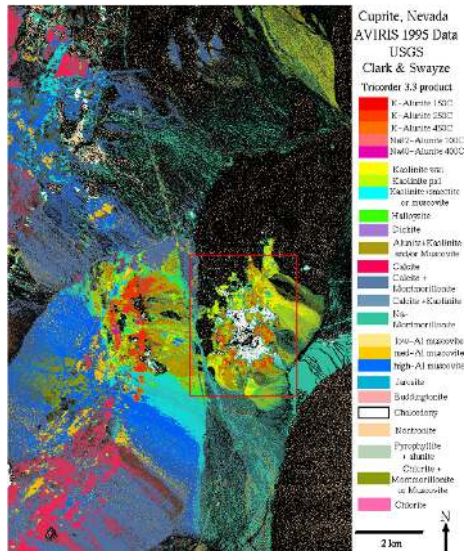


Fig. 6. USGS map showing the distribution of different minerals in Cuprite mining district in Nevada.

reduce the unmixing residuals for each pixel, i.e., optimize the abundances for each pixel as the iteration goes. In summary, the redesigned genetic and local search operators can overcome the optimization difficulties caused by the $L_{2,\infty}$ -norm-based residual objective.

4) *Brief Summary*: Our proposed Tp-MoSU+ is able to achieve comparable performance to Tp-MoSU and better performance than the regularization algorithms in estimating abundances, and it is more suitable for the highly noisy data because it can exploit more spatial-contextual information than Tp-MoSU to improve the quality of the estimated abundance. In addition, Tp-MoSU+ is relatively robust to the outliers and mismatches between hyperspectral data and the spectral library because of the elaborately redesigned genetic and local search operators.

C. Experiments on Real Hyperspectral Image

In this subsection, part of the well-known hyperspectral scene—airborne visible infra-red imaging spectrometer (AVIRIS) cuprite data²—is used to verify the proposed Tp-MoSU+. The portion (enclosed by the red rectangle in Fig. 6) used in our experiment corresponds to a subset with 250×191 pixels of the sector labeled f970619t01p02r02 in the online data.³ Considering the water absorption and low SNR, we removed the 1–2, 105–115, 150–170, and 223–224 bands, leaving a total number of 188 bands. Fig. 6 shows the distribution of materials in the cuprite dataset (detected in 1995) produced by the Tricorder 3.3 software. Because the available AVIRIS cuprite data used in this experiment were detected in 1997, the map shown in Fig. 6 can only be used as a reference for qualitative analysis of the materials.

Before unmixing, the USGS library is pruned with only 240 spectral signatures left because too much similar endmembers

TABLE X
EXECUTION TIME (S) OF ALL THE UNMIXING ALGORITHMS ON THE ABOVE THREE DATASETS

Algorithm	Data 1	Data 2	Cuprite (portion)
SUnSAL-TV	178.5	196.6	819.6
RSFoBa	7.6	23.2	65.9
SUnSPI	96.4	163.3	761.2
MUSIC-CSR	10.7	18.9	90.6
CSUnL0	1123	2457	8019
Tp-MoSU	436.9+34605.1	791.3+61970.4	2517.6+306173.2
Tp-MoSU+	1162.9+262.1	1956.6+490.9	6819.4+2918.5

will downgrade the unmixing performance, and the hyperspectral data are also preprocessed to eliminate mismatches between its spectra and the spectral library [20]. The number of estimated endmembers obtained in the first phase of Tp-MoSU+ is 11. Fig. 7 presents a qualitative comparison among the fractional abundances of the minerals: *Kaolinite wxl*, *Alunite+Kaolinite and/or Muscovite*, and *Jarosite* obtained by different algorithms. The parameters used in SUnSAL-TV, RSFoBa, SUnSPI, MUSIC-CSR, and CSUnL0 are tuned for better performance. Specifically, $(\lambda = 1e - 4, \lambda_{TV} = 1e - 4)$, $(\lambda = 1)$, $(\lambda_S = 1e - 4, \lambda_P = 1e - 3)$, $(\lambda_C = 0.01)$, and $(\lambda = 6 \times 10^{-5})$ for the above algorithms, respectively.

The Tricorder software analyzes hyperspectral data in a pixel level and marks each pixel with the most presentative material in it, so the abundance map of each material shown in Fig. 6 is keen-edged, but the comparison algorithms and the proposed Tp-MoSU+ attempt to interpret the hyperspectral data in a subpixel level and represent each pixel with several minerals, so the abundance map obtained by these algorithms are gradually varied. Therefore, the unmixing algorithms are able to obtain more realistic results than the Tricorder software. In addition, the dominated mineral in each pixel obtained by the unmixing algorithm is generally consistent with that identified by the Tricorder software. As can be seen from Fig. 7, our proposed Tp-MoSU+ is able to obtain comparable abundances to the comparison algorithms, and all the abundances obtained by these algorithms have their own highlights except for Tp-MoSU+(N), which does not converge completely.

D. Execution Time

The average execution time of the proposed method and comparison methods in 20 repeated times is presented in Table X, where the execution time of the two phases of Tp-MoSU and Tp-MoSU+ is listed separately with “+.” All the experiments are implemented by MATLAB 2014a software on a PC with a 3.20-GHz Intel CPU and 8-GB memory. Note that Tp-MoSU+ and Tp-MoSU can obtain 101 solutions in a single run, while the others only obtain one solution. Therefore, our proposed Tp-MoSU+ ranks the third among all the algorithms in terms of the average time per solution. Although the running time of the first phase of Tp-MoSU+ is two or three times that of Tp-MoSU because of the calculation of CSS measure, the second phase of Tp-MoSU+ is far more quickly than that of Tp-MoSU because it can estimate the abundance matrix in a single run and thus greatly reduces the time complexity.

²[Online]. Available: <http://aviris.jpl.nasa.gov/html/aviris.freedata.html>

³[Online]. Available: <http://www.lx.it.pt/%7Ebioucas/code/>

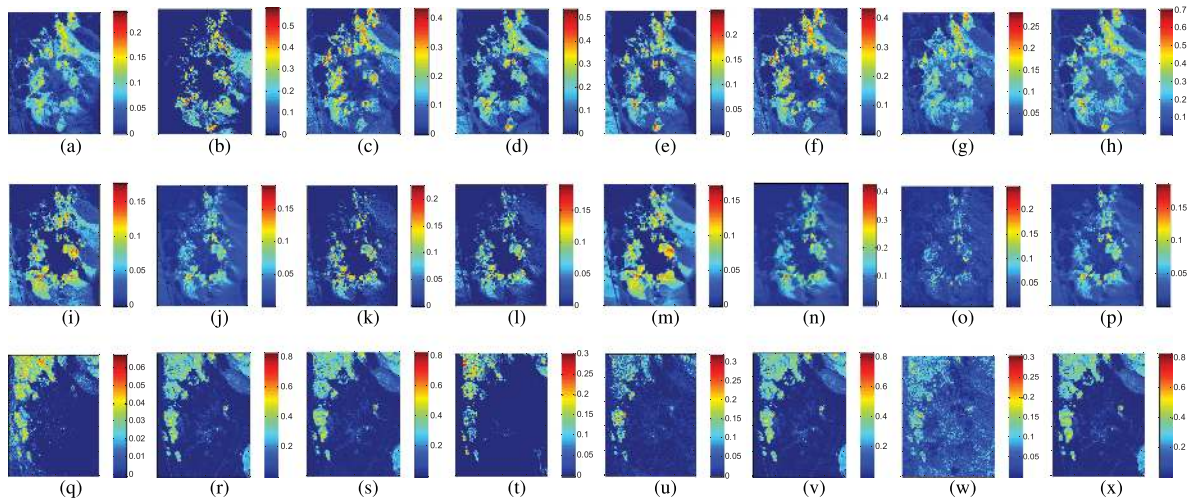


Fig. 7. Estimated abundances of the minerals: *Kaolinite wxl*, *Alunite+Kaolinite and/or Muscovite*, and *Jarosite* (from the top row to the bottom row) for the AVIRIS Cuprite data obtained by different algorithms (from the left to the right column: SuNSAL-TV, RSFoBa, SuNSPI, MUSIC-CSR, Tp-MoSU, CSUnL0, Tp-MoSU+(N), and Tp-MoSU+).

VI. CONCLUSION

This article focused on the limitations of Tp-MoSU method and proposed an effective Tp-MoSU+ method within the two-phase sparse unmixing framework. In the first phase, a CSS measure was constructed by fusing the SCA and Euclidean distance, which considers both the spectral shape and amplitude differences between spectra. In the second phase, an $L_{2,\infty}$ -norm-based residual objective was established, which aimed to facilitate the estimation of the abundances as a whole. The initialization, recombination, mutation, and local search strategies in the second phase were redesigned to accelerate the decrease of the unmixing residuals for all pixels efficiently.

Experimental results in the first phase demonstrated that the proposed Tp-MoSU+ outperformed Tp-MoSU in identifying the varying number of real endmembers from highly noisy data under spectral library with varying mutual coherence. Experimental results in the second phase demonstrated that the proposed Tp-MoSU+ could obtain visually better abundances than regularization algorithms and visually comparable abundances to Tp-MoSU under different noise levels. Furthermore, Tp-MoSU+ can estimate the abundance matrix as a whole and thus greatly reduce the time complexity and exploits more spatial-contextual information to improve the quality of the estimated abundance especially under heavy noise. Because of the advanced performance and the computational tractability, Tp-MoSU+ is an excellent choice for the HU tasks.

REFERENCES

- [1] N. Keshava and J. F. Mustard, "Spectral unmixing," *IEEE Signal Process Mag.*, vol. 19, no. 1, pp. 44–57, Jan. 2002.
- [2] N. M. Nasrabadi, "Hyperspectral target detection: An overview of current and future challenges," *IEEE Signal Process Mag.*, vol. 31, no. 1, pp. 34–44, Jan. 2014.
- [3] M. Fauvel, Y. Tarabalka, J. A. Benediktsson, J. Chanussot, and J. C. Tilton, "Advances in spectral-spatial classification of hyperspectral images," *Proc. IEEE*, vol. 101, no. 3, pp. 652–675, Mar. 2013.
- [4] G. S. Okin, D. A. Roberts, B. Murray, and W. J. Okin, "Practical limits on hyperspectral vegetation discrimination in arid and semiarid environments," *Remote Sens. Environ.*, vol. 77, no. 2, pp. 212–225, Aug. 2001.
- [5] P. Debba, F. Van Ruitenbeek, F. Van Der Meer, E. Carranza, and A. Stein, "Optimal field sampling for targeting minerals using hyperspectral data," *Remote Sens. Environ.*, vol. 99, no. 4, pp. 373–386, Dec. 2005.
- [6] H. Ren and C.-I. Chang, "Automatic spectral target recognition in hyperspectral imagery," *IEEE Trans. Aerosp. Electron. Syst.*, vol. 39, no. 4, pp. 1232–1249, Oct. 2003.
- [7] R. Pike, G. Lu, D. Wang, Z. G. Chen, and B. Fei, "A minimum spanning forest-based method for noninvasive cancer detection with hyperspectral imaging," *IEEE Trans. Biomed. Eng.*, vol. 63, no. 3, pp. 653–663, Mar. 2016.
- [8] C. P. Huynh and A. Robles-Kelly, "Hyperspectral imaging for skin recognition and biometrics," in *Proc. 17th IEEE Int. Conf. Image Process.*, 2010, pp. 2325–2328.
- [9] J. M. Bioucas-Dias *et al.*, "Hyperspectral unmixing overview: Geometrical, statistical, and sparse regression-based approaches," *IEEE J. Sel. Topics Appl. Earth Observ. Remote Sens.*, vol. 5, no. 2, pp. 354–379, Apr. 2012.
- [10] M.-D. Iordache, J. M. Bioucas-Dias, and A. Plaza, "Sparse unmixing of hyperspectral data," *IEEE Trans. Geosci. Remote Sens.*, vol. 49, no. 6, pp. 2014–2039, Jun. 2011.
- [11] S. Wang, T.-Z. Huang, X.-L. Zhao, G. Liu, and Y. Cheng, "Double reweighted sparse regression and graph regularization for hyperspectral unmixing," *Remote Sens.*, vol. 10, no. 7, 2018, Art. no. 1046.
- [12] J. Bieniarz, R. Muller, X. Zhu, and P. Reinartz, "On the use of overcomplete dictionaries for spectral unmixing," in *Proc. And Workshop Hyperspectral Image Signal Process., Evol. Remote Sens.*, 2012, pp. 1–4.
- [13] J. M. Bioucas-Dias and M. A. Figueiredo, "Alternating direction algorithms for constrained sparse regression: Application to hyperspectral unmixing," in *Proc. 2nd Workshop Hyperspectral Image Signal Process., Evol. Remote Sens.*, 2010, pp. 1–4.
- [14] J. M. Nascimento and J. M. Dias, "Vertex component analysis: A fast algorithm to unmix hyperspectral data," *IEEE Trans. Geosci. Remote Sens.*, vol. 43, no. 4, pp. 898–910, Apr. 2005.
- [15] J. Li, A. Agathos, D. Zaharie, J. M. Bioucas-Dias, A. Plaza, and X. Li, "Minimum volume simplex analysis: A fast algorithm for linear hyperspectral unmixing," *IEEE Trans. Geosci. Remote Sens.*, vol. 53, no. 9, pp. 5067–5082, Sep. 2015.
- [16] Y. Zhong, X. Wang, L. Zhao, R. Feng, L. Zhang, and Y. Xu, "Blind spectral unmixing based on sparse component analysis for hyperspectral remote sensing imagery," *ISPRS J. Photogramm. Remote Sens.*, vol. 119, pp. 49–63, 2016.
- [17] A. Zare and P. D. Gader, " L_1 -endmembers: A robust endmember detection and spectral unmixing algorithm," *Proc. SPIE*, vol. 7695, 2010, Art. no. 76951L.
- [18] M. Yong, L. Chang, X. Mei, C. Liu, and J. Ma, "Robust sparse hyperspectral unmixing with $l_{2,1}$ norm," *IEEE Trans. Geosci. Remote Sens.*, vol. 55, no. 3, pp. 1227–1239, Mar. 2017.
- [19] M.-D. Iordache, J. M. Bioucas-Dias, and A. Plaza, "Collaborative sparse unmixing of hyperspectral data," in *Proc. IEEE Int. Geosci. Remote Sens. Symp.*, Munich, Germany, 2012, pp. 7488–7491.

- [20] M.-D. Iordache, J. M. Bioucas-Dias, and A. Plaza, "Total variation spatial regularization for sparse hyperspectral unmixing," *IEEE Trans. Geosci. Remote Sens.*, vol. 50, no. 11, pp. 4484–4502, Nov. 2012.
- [21] R. A. Borsoi, T. Imbiriba, J. C. M. Bermudez, and C. Richard, "A fast multiscale spatial regularization for sparse hyperspectral unmixing," *IEEE Geosci. Remote Sens. Lett.*, vol. 16, no. 4, pp. 598–602, Apr. 2019.
- [22] Y. Zhong, R. Feng, and L. Zhang, "Non-local sparse unmixing for hyperspectral remote sensing imagery," *IEEE J. Sel. Topics Appl. Earth Observ. Remote Sens.*, vol. 7, no. 6, pp. 1889–1909, Jun. 2014.
- [23] R. Feng, Y. Zhong, and L. Zhang, "An improved nonlocal sparse unmixing algorithm for hyperspectral imagery," *IEEE Geosci. Remote Sens. Lett.*, vol. 12, no. 4, pp. 915–919, Apr. 2015.
- [24] L. Sun, C. Ma, Y. Chen, Y. Zheng, and B. Jeon, "Low rank component induced spatial-spectral kernel method for hyperspectral image classification," *IEEE Trans. Circuits Syst. Video Technol.*, vol. 30, no. 10, pp. 3829–3842, Oct. 2020.
- [25] R. Feng, Y. Zhong, L. Wang, and W. Lin, "Rolling guidance based scale-aware spatial sparse unmixing for hyperspectral remote sensing imagery," *Remote Sens.*, vol. 9, no. 12, Nov. 2017, Art. no. 1218.
- [26] L. Sun, F. Wu, T. Zhan, W. Liu, and B. Jeon, "Weighted nonlocal low-rank tensor decomposition method for sparse unmixing of hyperspectral images," *IEEE J. Sel. Topics Appl. Earth Observ. Remote Sens.*, vol. 13, pp. 1174–1188, Mar. 2020.
- [27] M. Gong, H. Li, E. Luo, J. Liu, and J. Liu, "A multiobjective cooperative coevolutionary algorithm for hyperspectral sparse unmixing," *IEEE Trans. Evol. Comput.*, vol. 21, no. 2, pp. 234–248, Apr. 2017.
- [28] X. Xu and Z. Shi, "Multi-objective based spectral unmixing for hyperspectral images," *ISPRS J. Photogramm. Remote Sens.*, vol. 124, pp. 54–69, Feb. 2017.
- [29] X. Xu, Z. Shi, and B. Pan, " l_0 -based sparse hyperspectral unmixing using spectral information and a multi-objectives formulation," *ISPRS J. Photogramm. Remote Sens.*, vol. 141, pp. 46–58, Jul. 2018.
- [30] X. Xu, Z. Shi, B. Pan, and X. Li, "A classification-based model for multi-objective hyperspectral sparse unmixing," *IEEE Trans. Geosci. Remote Sens.*, vol. 57, no. 12, pp. 9612–9625, Dec. 2019.
- [31] X. Xu, B. Pan, Z. Chen, Z. Shi, and T. Li, "Simultaneously multiobjective sparse unmixing and library pruning for hyperspectral imagery," *IEEE Trans. Geosci. Remote Sens.*, to be published, doi: [10.1109/TGRS.2020.3016941](https://doi.org/10.1109/TGRS.2020.3016941).
- [32] X. Jiang, M. Gong, H. Li, M. Zhang, and J. Li, "A two-phase multiobjective sparse unmixing approach for hyperspectral data," *IEEE Trans. Geosci. Remote Sens.*, vol. 56, no. 1, pp. 508–523, Jan. 2018.
- [33] Q. Zhang and H. Li, "MOEA/D: A multiobjective evolutionary algorithm based on decomposition," *IEEE Trans. Evol. Comput.*, vol. 11, no. 6, pp. 712–731, Dec. 2007.
- [34] J. Chen, X. Jia, W. Yang, and B. Matsushita, "Generalization of subpixel analysis for hyperspectral data with flexibility in spectral similarity measures," *IEEE Trans. Geosci. Remote Sens.*, vol. 47, no. 7, pp. 2165–2171, Jul. 2009.
- [35] O. A. Carvalho Jr., and P. R. Meneses, "Spectral correlation mapper (SCM): An improving spectral angle mapper," in *Proc. Annu. JPL Airborne Earth Sci. Workshop*, 2000, pp. 65–74.
- [36] D. D. Lee and H. S. Seung, "Algorithms for non-negative matrix factorization," in *Proc. Int. Conf. Neural Inf. Process. Syst.*, 2001, pp. 556–562.
- [37] L. Li, X. Yao, R. Stolkin, and M. Gong, "An evolutionary multiobjective approach to sparse reconstruction," *IEEE Trans. Evol. Comput.*, vol. 18, no. 6, pp. 827–845, Dec. 2014.
- [38] D. E. Goldberg, *Genetic Algorithms in Search, Optimization, and Machine Learning*. Reading, MA, USA: Addison-Wesley, 1989.
- [39] W. Tang, Z. Shi, and Y. Wu, "Regularized simultaneous forward-backward greedy algorithm for sparse unmixing of hyperspectral data," *IEEE Trans. Geosci. Remote Sens.*, vol. 52, no. 9, pp. 5271–5288, Sep. 2014.
- [40] W. Tang, Z. Shi, Y. Wu, and C. Zhang, "Sparse unmixing of hyperspectral data using spectral a priori information," *IEEE Trans. Geosci. Remote Sens.*, vol. 53, no. 2, pp. 770–783, Feb. 2015.
- [41] M.-D. Iordache, J. M. Bioucas-Dias, A. Plaza, and B. Somers, "MUSIC-CSR: Hyperspectral unmixing via multiple signal classification and collaborative sparse regression," *IEEE Trans. Geosci. Remote Sens.*, vol. 52, no. 7, pp. 4364–4382, Jul. 2014.
- [42] M.-D. Iordache, "A sparse regression approach to hyperspectral unmixing," Ph.D. dissertation, *School Elect. Comput. Eng.*, Inst. Superior Técnico, Lisboa, Portugal, Nov. 2011.



Xiangming Jiang received the B.S. degree in mathematics and applied mathematics and the Ph.D. degree in pattern recognition and intelligent systems from Xidian University, Xi'an, China, in 2015 and 2020, respectively.

He is currently a Lecturer with the School of Electronic Engineering, Xidian University. His research interests include computational intelligence and inverse problem in image understanding.



Maoguo Gong (Senior Member, IEEE) received the B.S. degree in electronic engineering and the Ph.D. degree in electronic science and technology from Xidian University, Xi'an, China, in 2003 and 2009, respectively.

Since 2006, he has been a Teacher with Xidian University. He was promoted to an Associate Professor and a Full Professor, in 2008 and 2010, respectively, both with exceptional admission. He has authored or coauthored more than 100 papers in journals and conferences, and holds more than 20 granted patents

as the first inventor. His research interests are broadly in the area of computational intelligence, with applications to optimization, learning, data mining, and image understanding.

Dr. Gong is leading or has completed more than 20 projects as the Principle Investigator, funded by the National Natural Science Foundation of China, the National Key Research and Development Program of China, and others. He was the recipient of the prestigious National Program for Support of the Leading Innovative Talents, the Leading Innovative Talent in the Science and Technology, the Excellent Young Scientist Foundation, the New Century Excellent Talent in University, the Young Teacher Award by the Fok Ying Tung Education Foundation, and the National Natural Science Award of China. He is the Executive Committee Member of Chinese Association for Artificial Intelligence and a Senior Member of Chinese Computer Federation, an Associate Editor or Editorial Board Member for more than five journals including the *IEEE TRANSACTIONS ON EVOLUTIONARY COMPUTATION* and *IEEE TRANSACTIONS ON NEURAL NETWORKS AND LEARNING SYSTEMS*.



Tao Zhan received the B.E. degree in electronic information engineering from the Henan University of Technology, Zhengzhou, China, in 2013 and the Ph.D. degree in pattern recognition and intelligent system from Xidian University, Xi'an, China, in 2019, respectively.

He is currently a Lecturer with the School of Computer Science and Technology, Xidian University. His research interests include computational intelligence and remote sensing image understanding.



Kai Sheng received the B.E. degree in information engineering from the Central South University, Changsha, China, in 2000 and Ph.D. degree in risk engineering from the University of Tsukuba, Tsukuba, Japan, in 2006.

He is currently a Professor with the School of Computer Science and Technology, Xidian University. His research interests include computational intelligence and remote sensing image understanding.



Mingliang Xu received the Ph.D. degree in computer science and technology from the State Key Laboratory of CAD&CG, Zhejiang University, Hangzhou, China, in 2012.

He is currently a Professor with the School of Information Engineering, Zhengzhou University, Zhengzhou, China. He has authored more than 60 journal articles and conference papers, including those published in the *ACM Transaction on Graphics*, *IEEE TRANSACTIONS ON PATTERN ANALYSIS AND MACHINE INTELLIGENCE*, *IEEE TRANSACTIONS ON*

IMAGE PROCESSING, *IEEE TRANSACTIONS ON CIRCUITS AND SYSTEMS FOR VIDEO TECHNOLOGY*, *ACM Special Interest Group on Computer Graphics, Asia/ACM Multimedia Conference*, and the *IEEE International Conference on Computer Vision*. His current research interests include computer graphics, multimedia, and artificial intelligence.